Monthly Notices
of the
ROYAL ASTRONOMICAL SOCIETY

MNRAS **455,** 2028–2041 (2016) doi:10.1093/mnras/stv2400

MUSE sneaks a peek at extreme ram-pressure stripping events – II. The physical properties of the gas tail of ESO137−001

Matteo Fossati,[1,2]★ Michele Fumagalli,[3] Alessandro Boselli,[4] Giuseppe Gavazzi,[5] Ming Sun[6] and David J. Wilman[1,2]

[1]*Universitäts-Sternwarte München, Scheinerstrasse 1, D-81679 München, Germany*
[2]*Max-Planck-Institut für Extraterrestrische Physik, Giessenbachstrasse, D-85748 Garching, Germany*
[3]*Institute for Computational Cosmology and Centre for Extragalactic Astronomy, Department of Physics, Durham University, South Road, Durham DH1 3LE, UK*
[4]*Aix Marseille Université, CNRS, LAM (Laboratoire d' Astrophysique de Marseille) UMR 7326, F-13388 Marseille, France*
[5]*Universitá di Milano-Bicocca, piazza della Scienza 3, I-20100 Milano, Italy*
[6]*Department of Physics, University of Alabama in Huntsville, Huntsville, AL 35899, USA*

Accepted 2015 October 14. Received 2015 October 13; in original form 2015 August 17

ABSTRACT

We present a study of the physical properties of the disc and tail of ESO137−001, a galaxy suffering from extreme ram-pressure stripping during its infall into the Norma cluster. With sensitive and spatially resolved MUSE (Multi Unit Spectroscopic Explorer) spectroscopy, we analyse the emission line diagnostics in the tail of ESO137−001, finding high values of [N II]/Hα and [O I]/Hα that are suggestive of the presence of shocks in turbulent gas. However, the observed line ratios are not as strong as commonly seen in pure shock heating models, suggesting that other emission mechanisms may contribute to the observed emission. Indeed, part of the observed emission, particularly at close separations from the galaxy disc, may originate from recombination of photoionized gas stripped from the main body of ESO137−001. We also identify a large number of bright compact knots within in the tail, with line ratios characteristic of H II regions. These H II regions, despite residing in a stripped gas tail, have quite typical line ratios, densities, temperatures, and metallicity (∼0.7 solar). The majority of these H II regions are embedded within diffuse gas from the tail, which is dynamically cool ($\sigma \sim 25$–50 km s^{-1}). This fact, together with a lack of appreciable gradients in age and metallicity, suggests that these H II regions formed *in situ*. While our analysis represents a first attempt to characterize the rich physics of the ESO137−001 tail, future work is needed to address the importance of other mechanisms, such as thermal conduction and magnetohydrodynamic waves, in powering the emission in the tail.

Key words: shock waves – techniques: spectroscopic – H II regions – galaxies: abundances – galaxies: clusters: individual: ESO137−001 – galaxies: ISM.

1 INTRODUCTION

It has long been known that galaxy colour and morphology correlate both with local environment and stellar mass (Dressler 1980; Kennicutt 1983; Postman & Geller 1984; Bell et al. 2004; Peng et al. 2010), an empirical manifestation that both internal and external physical processes play an important role in shaping the star formation of galaxies at all cosmic ages (see e.g. Boselli & Gavazzi 2006; Blanton & Moustakas 2009). Many studies point to internal processes, which often correlate with stellar or bulge mass, as key drivers for quenching star formation activity at all densities (Cowie et al. 1996; Gavazzi, Pierini & Boselli 1996; Mendel et al. 2013; Wilman et al. 2013; Lang et al. 2014). However, the advent of large-scale surveys has also highlighted and strengthened earlier findings that environmental effects in rich clusters and groups are key drivers for the quenching of star formation (Balogh et al. 2004; Baldry et al. 2006; Boselli & Gavazzi 2006, 2014; Weinmann et al. 2006; Gavazzi et al. 2010; Wilman, Zibetti & Budavári 2010; Mok et al. 2013).

In this respect, rich galaxy clusters are the best laboratories for investigating the processes that are responsible for quenching star formation, due to the combination of strong potential wells, high number density of galaxies, and the presence of the intracluster

★ E-mail: mfossati@mpe.mpg.de

medium (ICM), a hot and dense plasma filling the intergalactic space. Several mechanisms have been proposed as the culprit for galaxy transformation within clusters, including tidal interactions between galaxies (sometimes called galaxy harassment) or with the cluster potential itself (Byrd & Valtonen 1990; Henriksen & Byrd 1996; Moore et al. 1996), galaxy strangulation (Larson, Tinsley & Caldwell 1980), and ram-pressure stripping (Gunn & Gott 1972).

Although more than one of these mechanisms likely play a role in the evolution of cluster galaxies at one time, a few pieces of observational evidence consistently point to ram-pressure stripping as a widespread process, and one of crucial importance for the transformation of low-mass galaxies that are being accreted on to clusters at recent times (Boselli et al. 2008). Observationally, the fingerprint of ram pressure is the removal of the galaxy gas content without inducing strong disturbances in the older stellar populations. Indeed, large radio surveys have found that the H I content of cluster (and to some extent group) galaxies is being reduced with respect to their field counterparts (Giovanelli & Haynes 1985; Solanes et al. 2001; Cortese et al. 2011; Fabello et al. 2012; Catinella et al. 2013; Gavazzi et al. 2013; Jaffé et al. 2015), an effect that has been also recently observed in the molecular phase (Fumagalli et al. 2009; Boselli et al. 2014). This gas depletion, in turn, induces truncated profiles in young stellar populations compared to old ones (Boselli et al. 2006; Koopmann, Haynes & Catinella 2006; Cortese et al. 2012; Fossati et al. 2013).

Besides understanding the influence of ram pressure on cluster galaxies as a population, a detailed look at how this mechanism operates on small scales within individual galaxies is becoming a pressing issue, so as to gain insight into how gas removal occurs as a function of parameters such as galaxy mass or distance from the cluster centre. Also poorly understood is the fate of the stripped gas, which could mix with the hotter ICM or cool again to form stars, thus contributing to the intracluster light. Fortunately, these detailed investigations are now within reach, thanks to the advent of integral field spectrographs at large telescopes.

Ram pressure has been caught in the act by searching for UV and Hα tails downstream of galaxies in fast motion through massive clusters like Coma or Virgo (Gavazzi et al. 2001; Yoshida et al. 2002; Cortese et al. 2006; Kenney et al. 2008; Smith et al. 2010; Yagi et al. 2010; Fossati et al. 2012). The amount of star formation in stripped tails has been the subject of several analyses, both from the observational (Smith et al. 2010; Yagi et al. 2010; Fumagalli et al. 2011; Arrigoni Battaia et al. 2012; Boissier et al. 2012; Fossati et al. 2012) and theoretical point of view (e.g. Kapferer et al. 2009; Tonnesen & Bryan 2012). However, the efficiency of star formation and its dependence on the gas properties of the tails remain poorly understood.

A poster child for studies of ram-pressure stripping is ESO137−001, a spiral galaxy near the core of the Norma cluster. The Norma cluster, also known as A3627, has a dynamical mass of $M_{\rm dyn} \sim 10^{15}\,{\rm M}_{\odot}$ at a redshift $z_{\rm cl} = 0.016\,25 \pm 0.00018$ (Woudt et al. 2008; Nishino, Fukazawa & Hayashi 2012). ESO137−001 is located at a projected distance of only ∼267 kpc from the central cluster galaxy, and features a wealth of multiwavelength observations ranging from X-ray to radio wavelengths (Sun et al. 2006, 2010; Sun, Donahue & Voit 2007; Sivanandam, Rieke & Rieke 2010; Jachym et al. 2014).

All these observations clearly show that ESO137−001 is suffering from extreme ram-pressure stripping, arguably during its first infall into the cluster environment. Indeed, while ESO137−001 can be classified as a normal spiral galaxy from its stellar continuum, X-ray and Hα observations reveal the presence of a double tail that extends for ∼80 kpc behind the galaxy disc, in the opposite direction from the cluster centre (Sun et al. 2006, 2007, 2010). These tails are believed to originate from the hydrodynamic interaction between the hot ICM and the cold interstellar medium (ISM), which is removed from the galactic disc (Sun et al. 2007; Fumagalli et al. 2014; Jachym et al. 2014). Although stripped tails have been extensively studied in imaging in various nearby clusters, the number of spectroscopic studies in the optical has been limited in the past (e.g. Yagi et al. 2007; Yoshida et al. 2012; Merluzzi et al. 2013), due to the extended nature and the low surface brightness of the emitting regions.

To overcome the lack of extended spectroscopic follow-up of this galaxy, we have collected integral field spectroscopic observations of ESO137−001 following the deployment of Multi Unit Spectroscopic Explorer (MUSE; Bacon et al. 2010) at the ESO Very large Telescope. These observations have been presented in the first paper of this series (Fumagalli et al. 2014, hereafter Paper I). The combination of high efficiency, spectral resolution, and large field of view of MUSE have allowed us to map the kinematics of the stripped tail for the first time. In Paper I, we found that the stripped gas retains the imprint of the disc rotational velocity up to ∼20 kpc downstream, with low velocity dispersion. Further on along the tail, the gas velocity dispersion increases up to ∼100 km s^{-1}. Moreover, we observed an ordered velocity field for the stellar disc, which convincingly points to ram pressure as the mechanism for gas removal.

In this paper, we extend our previous analysis by investigating the physical properties of the ionized gas and the star formation in the tail of ESO137−001 by means of multiple emission line diagnostics. The structure of this paper is as follows. After discussing an improved data reduction scheme for MUSE observations (Section 2) and the data analysis technique (Section 3), we present a study of the emission line ratios as diagnostic of the physical conditions of the gas in the tail (Section 4). Lastly, we focus on several H II regions detected throughout the tail, and briefly discuss possible formation mechanisms. Throughout this paper, we adopt a standard Λ cold dark matter cosmology with $H_0 = 69.7$ and $\Omega_{\rm m} = 0.236$ (Hinshaw et al. 2013). With the adopted cosmology, 1 arcsec corresponds to 0.32 kpc at the distance of ESO137−001.

2 OBSERVATIONS AND DATA REDUCTION

ESO137−001 was observed with MUSE during the science verification programme 60.A-9349(A) on 2014 June 21. The details of the observational setup are presented in Paper I, and they are only briefly summarized here. Observations were acquired in photometric conditions and under good seeing (0.7–0.8 arcsec), using the Wide Field Mode with nominal wavelength coverage (4800–9300 Å). The spectral resolution is ∼50 km s^{-1} and roughly constant across the wavelength range. The raw data have been processed with the MUSE data reduction pipeline (v 0.18.1), which we supplemented with custom-made IDL codes to improve the quality of the illumination correction and of the sky subtraction. As discussed in Paper I, we first apply to each exposure an illumination correction, which we obtain by comparing the brightness of multiple sky lines to compensate for variations in the response of the different MUSE spectrographs.

After this step, we perform sky subtraction using in-house codes, as the very crowded nature of our field requires additional processing to avoid large negative residuals, as shown in Fig. 1. In this work, we further improve on the method adopted in Paper I, so as to maximize the quality of the sky subtraction across the entire wavelength range of the data cube. In particular, because a significant fraction of

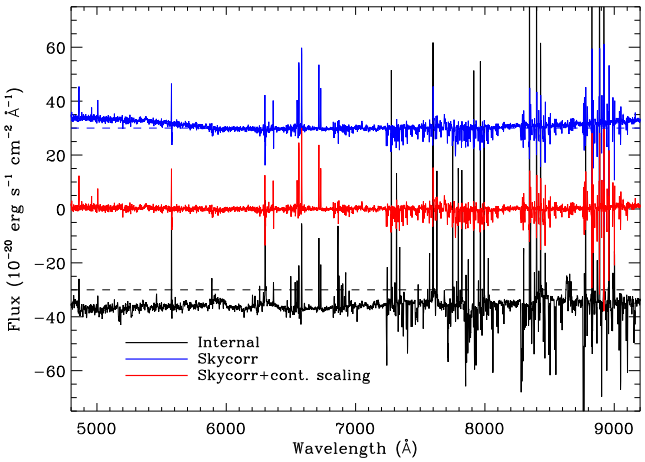

Figure 1. Sky residuals recorded in a 10 pixel square aperture within one science exposure that has been processed with different algorithm for sky subtraction. The black line shows the result of the MUSE pipeline in this crowded field. The blue line is obtained by subtracting a sky model derived from a second sky exposure together with the scaling computed with SKYCORR. Both spectra are visibly offset from the zero level, marked by the dashed lines. The red line shows the sky residual in the data cube, after including scaling in both the airglow lines and the continuum to match the level recorded in the science exposure. Large sky line residuals do not appear in the final processed cube (the group of lines at ∼6500 Å, whose residuals do not change in the three spectra, are in fact emission lines from the Galaxy).

our field is filled by the emission lines from the tail of ESO137−001 or by the continuum emission from the stellar disc and halo, we use exposures of empty sky regions to avoid the inclusion of spurious signal arising from the galaxy itself in the sky model. Specifically, we use a sky exposure of 60 s, acquired ∼1 h apart from our science observations by the programme 60.A-9303(A).

As a first step, we generate a supersampled sky spectrum (hereafter the sky model) after processing the pixel table of the sky exposure with the same pipeline recipes used for our science exposures. This sky model, however, cannot be directly subtracted from the science exposures because of the time dependence of both the airglow line and continuum fluxes. To correct for this variation, we exploit the ESO tool SKYCORR (Noll et al. 2014) to compute a physically motivated scaling of the airglow lines in the sky model to match the levels recorded in a model spectrum extracted from each of the science exposures. Empirically, we find that SKYCORR produces line models which yield small residuals after subtraction, as shown in Fig. 1. At this stage, however, SKYCORR does not attempt any scaling of the sky continuum emission, mainly because the continuum emission from the sources cannot be easily separated from the sky continuum level. Thus, to set a zero-point for the sky continuum emission, we take advantage of the large field of view of MUSE which contains regions that are not affected by the galaxy's continuum flux. After subtracting the rescaled sky model from the science exposures, any residual deviation from a zero continuum level in these 'empty' regions arises because of the different sky continuum level in the science and the sky exposures (see Fig. 1). To remove this last signature, we fit two third-degree polynomials in regions free from sky lines above and below 6200 Å, that is the wavelength where the sky continuum reaches its peak. Finally, we use this polynomial fit to correct for the residuals due to varying sky continuum emission (Fig. 1). During these steps, the sky model is subtracted from each pixel of the data cube by interpolating on the wavelength axis with a spline function. The appropriate uncertainties are added to the variance stored in the data cube (the 'stat' extension).

After sky subtraction, we use the MUSE pipeline to combine the four individual exposures and reconstruct the final data cube on a regular grid of 0.2 arcsec in the spatial direction and 1.25 Å in the spectral direction. As a last step, we apply the heliocentric correction and we correct the observed flux as a function of wavelength to account for a substantial amount of Galactic extinction in the direction of ESO137−001. This correction is computed using the colour excess from the dust map by Schlegel, Finkbeiner & Davis (1998) with the recalibration of Schlafly & Finkbeiner (2011). We also assume a Galaxy extinction curve from Fitzpatrick (1999).

In Paper I, we have verified the accuracy of the flux calibration by comparing the Hα fluxes of selected H II regions to the measurements reported by Sun et al. (2007). We further verify that the flux calibration is consistent across the entire wavelength range by checking that the spectra of stars in the field are well fitted by blackbody functions. Moreover, we compare the flux ratios of several emission lines derived in this work to those from Sun et al. (2010) for their H II regions ELO2 and ELO7, finding agreement within 5 per cent for all the flux ratios compared.

3 EMISSION LINE MEASUREMENTS

To characterize the physical properties of the gas in the disc and the tail, we extract flux maps of the emission lines listed in Table 1. In this table, we also provide for each line an estimate of the noise, quantified as the 3σ limit per spaxel in the unsmoothed MUSE data cube. As in Paper I, we assume a systemic redshift $z_{\rm sys} = 0.01555 \pm 0.00015$ for ESO137−001. Maps of the line fluxes are obtained from the reduced data cube using the IDL custom code KUBEVIZ. Before the fit, the data cube is median filtered in the spatial direction with a kernel of 15 × 15 pixels (corresponding to 3 arcsec or 0.95 kpc at the distance of ESO137−001) to increase the signal-to-noise (S/N) per pixel without compromising the spatial resolution of the data. No spectral smoothing is performed.

In the galaxy disc, Balmer emission lines (Hα and Hβ) are contaminated by stellar absorption. Direct fitting of the emission lines would thus underestimate the fluxes. To solve this problem, we first model and subtract the underlying galaxy stellar continuum using

Table 1. Emission lines considered in this study. The columns of the table are (1) name of the emission line; (2) wavelength in air; (3) characteristic surface brightness limit at 3σ C. L. computed in each spaxel after correcting for Galactic extinction. The two values refer to pointings A and B, respectively.

Line	$\lambda_{\rm r}$ (Å)	$\mu_{\rm min}$ (erg s^{-1} cm^{-2} A^{-1} arcsec^{-2})
Hβ	4861.33	8.2–11.7 × 10^{-18}
[O III]	4958.91	7.7–10.7 × 10^{-18}
[O III]	5006.84	7.5–10.5 × 10^{-18}
[N II]	5754.64	6.2–8.7 × 10^{-18}
[O I]	6300.30	4.6–6.3 × 10^{-18}
[O I]	6363.78	5.0–6.7 × 10^{-18}
[N II]	6548.05	4.1–5.6 × 10^{-18}
Hα	6562.82	4.1–5.6 × 10^{-18}
[N II]	6583.45	4.1–5.5 × 10^{-18}
[S II]	6716.44	4.9–6.4 × 10^{-18}
[S II]	6730.81	5.0–6.6 × 10^{-18}
[S III]	9068.60	4.8–6.9 × 10^{-18}

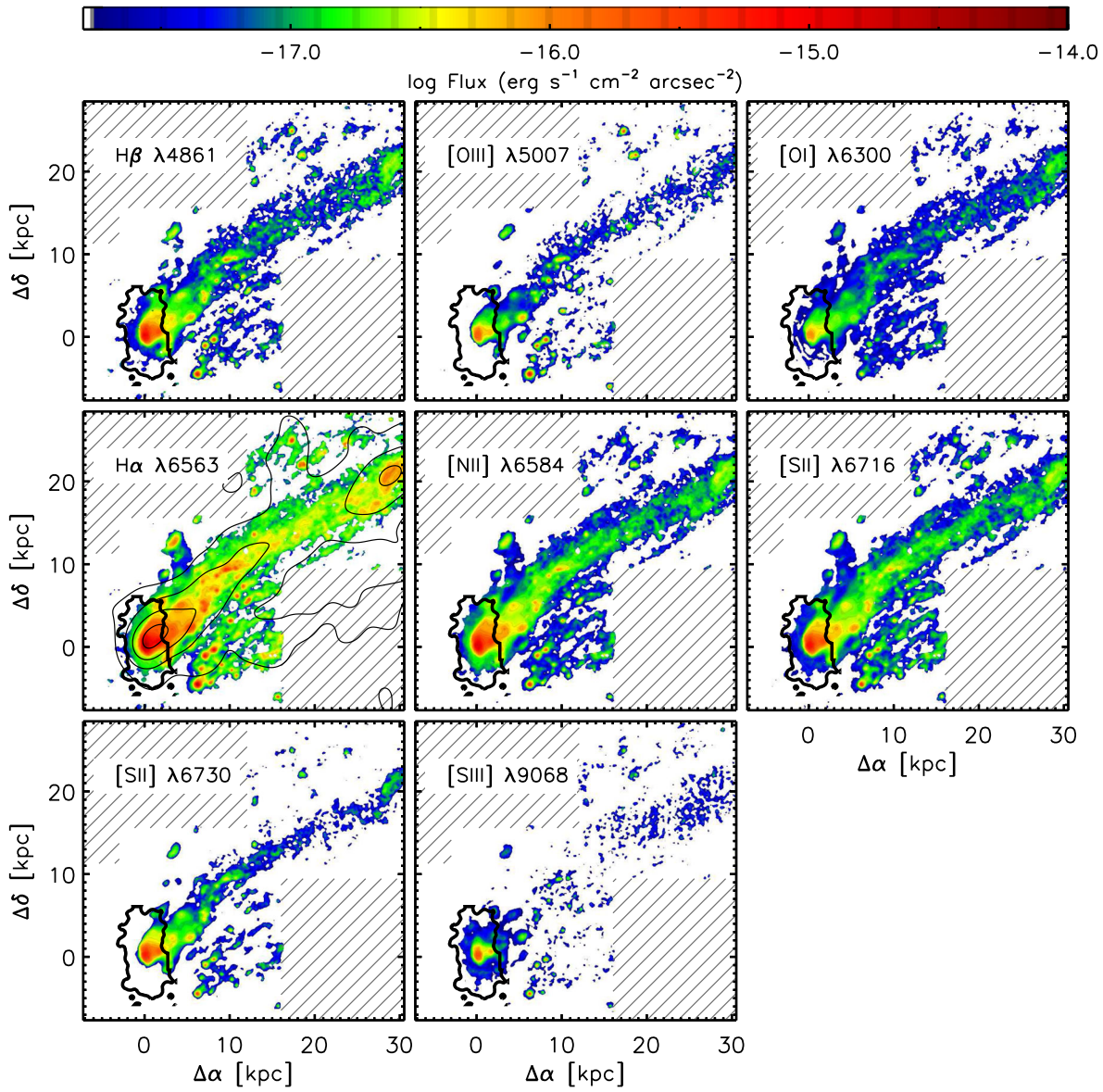

Figure 2. Emission line maps of ESO137−001. The panels are sorted by the wavelength of the line from left to right and top to bottom. The black solid contour marks the isophote of the galactic disc at 22 mag arcsec^{-2} measured on an *r*-band image obtained from the data cube. The thinner solid contours in the Hα panel show the location of the X-ray emitting gas from *Chandra* observations (Sun et al. 2010), highlighting the primary and secondary tails. Areas not covered by MUSE observations are shaded in grey.

the GANDALF code (Sarzi et al. 2006) for spaxels in a rectangular area that covers the stellar disc (see fig. 5 in Paper I) and with S/N > 5 per velocity channel in the continuum. GANDALF works in combination with the Penalized Pixel-Fitting code (Cappellari & Emsellem 2004) to simultaneously model the stellar continuum and the emission lines in individual spaxels. The stellar continuum is modelled with a superposition of stellar templates convolved by the stellar line-of-sight velocity distribution, whereas the gas emission and kinematics are derived assuming a Gaussian line profile. To construct the stellar templates, we use the MILES library (Vazdekis et al. 2010).

Having obtained a data cube free from underlying stellar absorption, we use KUBEVIZ[1] to fit the emission lines. This code uses 'linesets', defined as groups of lines that are fitted simultaneously. Each lineset (e.g. Hα and [N II] $\lambda\lambda$6548, 6584) is described by a combination of 1D Gaussian functions where the relative velocity separation of the lines is kept fixed according to the wavelengths listed in Table 1. To facilitate the convergence of the fit for the faintest lines, we impose a prior on the velocity and the intrinsic line width σ of each lineset, which is fixed to that obtained fitting the Hα and [N II] lines. We have explicitly verified on the master spectra described in Section 4 that this assumption holds well both in the disc and across the tail. Furthermore, the flux ratios of the two [N II] and [O III] lines are kept constant in the fit to the ratios in Storey & Zeippen (2000). The continuum level is evaluated inside two symmetric windows around each lineset. Fig. 2 shows emission line maps obtained from our fits of the data cube at selected wavelengths. We note that, at the redshift of ESO137−001, [S II] λ6731 falls on to a bright sky line at λ6834 and thus the strong

[1] http://www.mpe.mpg.de/~mfossati/kubeviz

residual hampers a reliable estimate of the flux for this line (see Fig. 5). Therefore, we are forced to exclude [S II] from most of the following analysis.

During the fit, KUBEVIZ takes into account the noise from the 'stat' data cube, thus optimally suppressing sky line residuals. However, the adopted variance underestimates the real error, most notably because it does not account for correlated noise introduced by resampling and smoothing. We therefore renormalize the final errors on the line fluxes assuming a $\chi^2 = 1$ per degree of freedom. In the end, as in Paper I, we mask spaxels where the S/N in the Hα line is <3. Further masking is applied to the spaxels for which the line centroids or the line widths are extreme outliers compared to the median value of their distributions, or the errors on these quantities exceed 50 km s^{-1}.

4 EMISSION LINE DIAGNOSTICS

Several physical processes, including photoionization, shocks, and thermal energy in mixing layers, are likely to contribute to the emission lines we see in the spectra of the main body of ESO137−001 and its tail. In this work, we primarily focus on the photoionization and shocks. In a forthcoming paper, new observations (095.A-0512(A)) covering the full extent of the primary and the secondary tails will be used in combination with multiwavelength data to study the interaction between the warm ionized gas in the tail and the hot ICM.

4.1 Line ratio maps

In this section, we exploit the integral field capabilities of MUSE to investigate the spatial variations of physical properties inferred from strong emission line diagnostics computed for each pixel. Next, we will co-add the spectra of several characteristic regions of the ESO137−001 system to achieve higher S/N in the fainter lines.

The ratio of collisionally excited lines like [O III] λ5007, [N II] λ6584 to hydrogen recombination lines (Hα, Hβ) is traditionally used as indicator of the ionization properties of the gas. More specifically, the combination of pairs of these line ratios is used to construct BPT diagrams (Baldwin, Phillips & Terlevich 1981), so as to distinguish different sources of ionization, e.g. photoionization in star-forming galaxies or active galactic nuclei, and shocks. These line ratios are typically chosen such that both lines fall inside a small window of wavelength to minimize the effects of dust extinction.

The top panels of Fig. 3 show 2D maps of the [O III] λ5007/Hβ, [N II] λ6584/Hα, and [O I] λ6300/Hα ratios, computed for all the spaxels in which both of the lines of interest are detected with S/N > 3. Significant spatial variations in these three line ratios can be seen in the data. Most of the large-scale trends visible in this figure are real, but we caution that two effects should be taken into account when interpreting the maps. First, in the outer tail, the depth of the observations is shallower due to shorter exposure time. Secondly, in the front region, the smoothing applied to the data cube can artificially enhance discontinuities in line ratios and affect their gradients.

Inspecting the Hα map (left central panel in Fig. 2), compact knots along the tail can be identified as high-surface-brightness regions. To isolate these knots, we run SExtractor v2.19.5 (Bertin & Arnouts 1996) on the Hα map. Among the detected objects (S/N > 5), we selected those with a classification consistent with point-like sources (CLASS_STAR > 0.9) and low ellipticity (e < 0.2). 33 such knots are identified in our data. Out of these 27 correspond to the H II regions analysed in Sun et al. (2007, 2010). The remaining six regions lie close to foreground stars, making their selection more difficult in the narrow-band imaging data of Sun et al. (2007). In Fig. 3, we have highlighted the position the compact knots with black circles. These regions are mainly characterized by high values of [O III] λ5007/Hβ ($\gtrsim$0.7) as well as low values of [N II] λ6584/Hα ($\lesssim$0.3) and [O I] λ6300/Hα ($\lesssim$0.1) ratios. According to the BPT classification (see also Fig. 7), all these regions occupy the parameter space populated by H II regions photoionized by OB stars.

Focusing next on the galaxy nucleus, at the origin of the coordinate system in Fig. 3, we see modest ratios for [O III] λ5007/Hβ, [N II] λ6584/Hα, and [O I] λ6300/Hα, which is again consistent with ionization from a soft spectral energy distribution. Thus, in agreement with the X-ray analysis of Sun et al. (2010), we conclude that the nuclear emission of ESO137−001 is powered by star formation activity and that this galaxy does not host a strong AGN.

Looking at the galaxy front next, where the ISM collides with the hot plasma from the cluster, we see enhanced [N II] λ6584/Hα ($\gtrsim$0.6) as well as low [O III] λ5007/Hβ ($\lesssim$0.3), with a hint of elevated [O I] λ6300/Hα. These ratios are suggestive of shocks playing a role in the gas excitation (Allen et al. 2008; Rich, Kewley & Dopita 2011). Throughout the primary tail, [N II] λ6584/Hα remains elevated (∼0.4) decreasing only towards the end of the tail, in proximity of the extended Hα blob that is known to harbour a large molecular complex (Jachym et al. 2014). We also find enhanced [O I] λ6300/Hα ($\gtrsim$0.2) in the tail, while the [O I] line is weaker in the galactic disc. This piece of evidence, combined with the high gas turbulence measured in Paper I, points to shock heating as an important mechanism to excite the gas in the tail.

Differently from the primary tail, the southern secondary tail shows a strong [O I] emission, but a lower [N II] λ6584/Hα, which is on average ∼0.2 after removing the H II regions. These line ratios are more difficult to reconcile with emission lines from ordinary shock models. We note however that the presence of several bright H II regions embedded in this tail can produce mixed types of spectra, with a superposition of emission lines that originate from different emission mechanisms in distinct gas phases. More generally, we are witnessing a complex interaction between multiple gas phases as the warm ISM from the galaxy, ionized by past and ongoing star formation, mixes and interacts with the hot ICM. Thus, photoionization from stars, shocks, and even thermal conduction and magnetohydrodynamic (MHD) waves (see e.g. Ferland et al. 2008, 2009), are likely contributing to a varying degree to the peculiar line ratios seen in ESO137−001.

We conclude this section by briefly commenting on the Hα/Hβ ratio, shown in the fourth panel of Fig. 3. This ratio is commonly used in the low density limit to infer the dust extinction, assuming an intrinsic ratio of 2.86 from case B recombination at $T = 10^4$ K (Osterbrock 1989). As the observed emission, especially in the tail, may not simply arise from photoionized gas at the temperature of typical H II regions (see Section 4.2), we refrain from deriving a spatially resolved map for the extinction. We only note that ratios are generally Hα/H$\beta \gtrsim 3$, which is suggestive of the presence of dust both in the disc and tail of ESO137−001. Cortese et al. (2010a,b) indeed observed dust stripping from galaxies in cluster environments, supporting the idea that gas and dust are subject to similar perturbations.

4.2 Composite spectra

Having examined qualitatively the spatial variation of the different line ratios, in this section we exploit the ability to rebin IFU data in regions of interest. We generate high-S/N composite spectra for a

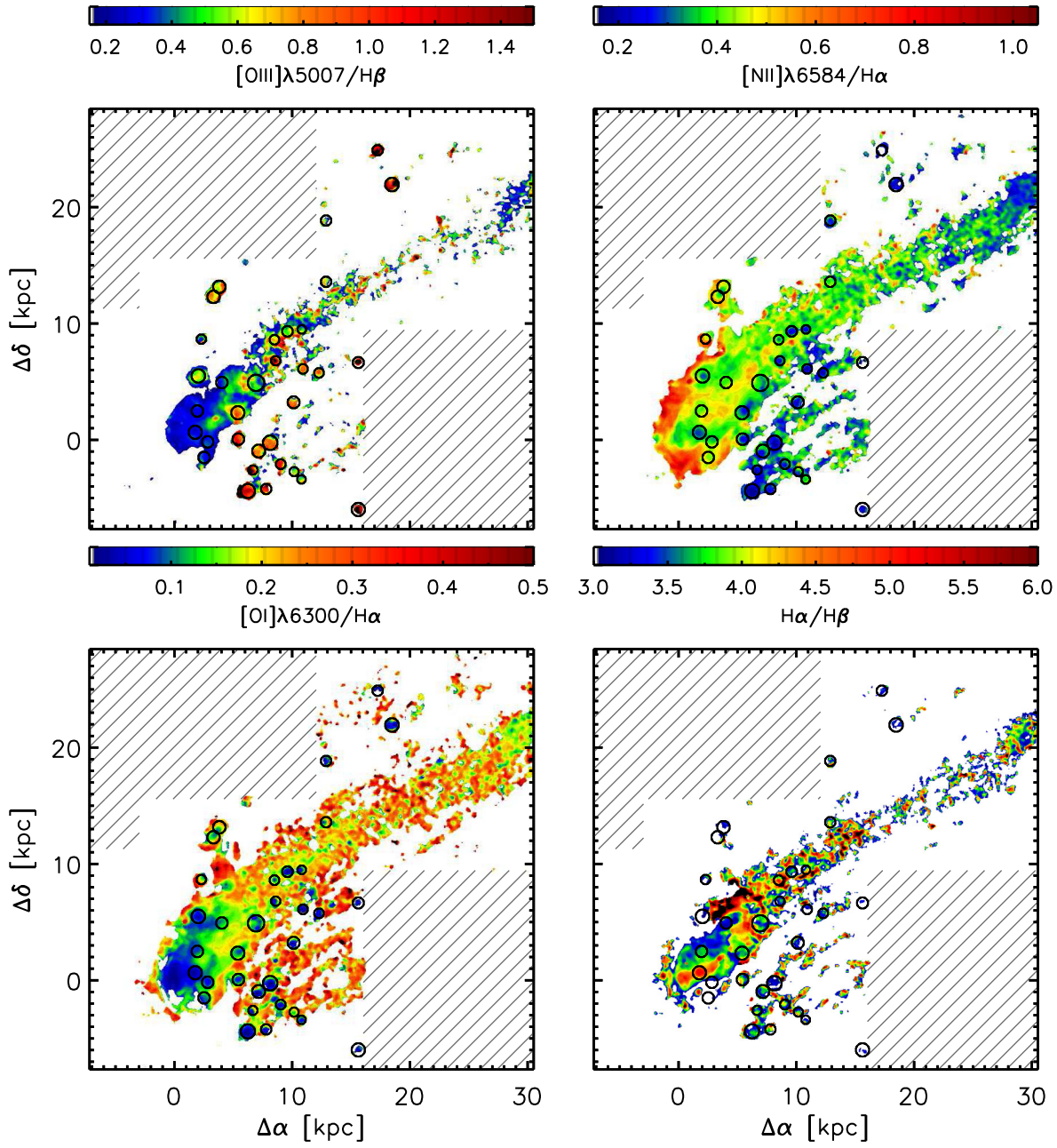

Figure 3. Maps of the [O III] λ5007/Hβ, [N II] λ6584/Hα, [O I] λ6300/Hα, and Hα/Hβ line ratios. Areas not covered by MUSE observations are shaded in grey. The compact knots associated with H II regions along the tail are highlighted with black circles in all the panels.

quantitative analysis of even weak emission lines. We focus on five characteristic regions, which exhibit different line ratios in Fig. 3. These are (1) the galaxy disc, including the nucleus; (2) the front region, defined as the area with enhanced [N II]/Hα ratio in the south-east of the galaxy disc; (3) the compact knots along the tail, which we have identified as H II regions; (4) the diffuse gas within the primary tail; (5) the Hα 'blob' in the outer tail.

The locations of these different regions are shown in Fig. 4, while Fig. 5 shows the composite spectra obtained by co-adding all spaxels in the selected apertures with a mean. Before generating the composite spectra, we remove the velocity offsets due to the systemic redshift differences that arise because of the galaxy rotation. For these corrections, we rely on the gas velocity field derived on the new reduction with the methods described in Paper I.

For the regions 1 and 2, we further use the GANDALF code to remove the stellar continuum spectrum from the composite spectrum, as described above. The composite spectrum of the H II regions is instead obtained by averaging the individual spectra with inverse variance weights derived from the bootstrap noise spectra described below.

Fig. 5 reveals that the wavelength at which all the emission lines peak is consistent with the galaxy's redshift regardless of the transition under consideration. The largest offsets occur predominantly in the regions where the lines are fainter, but these are generally consistent with zero given the uncertainties on the line centroid. This empirical evidence justifies our previous assumption to peg the centroid of different emission lines to the one of Hα when deriving the flux maps in the full data cube.

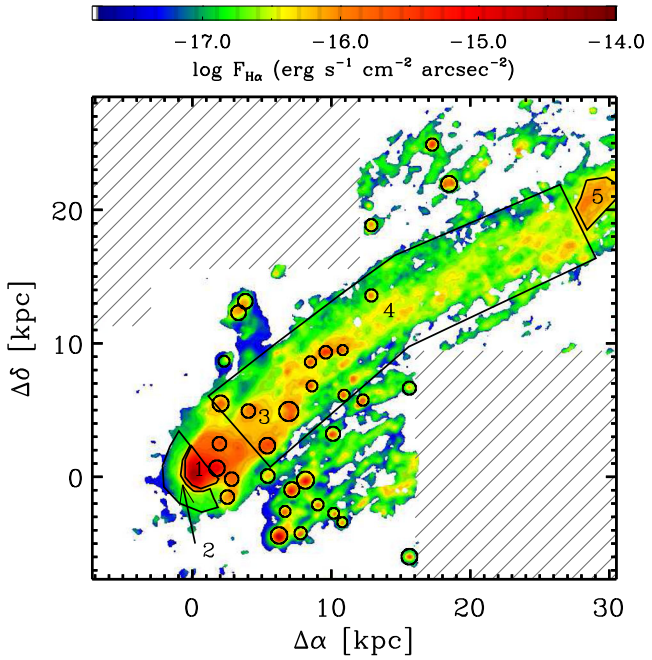

Figure 4. Hα map of ESO137−001. Black apertures represent selected regions used to create composite spectra as described in the text. Specifically, circular apertures identify H II regions (3), while polygons identify (from left to right): the front region (2); the main body of the galaxy (1); the diffuse gas within the tail (4); the blob in the outer tail (5). Areas not covered by MUSE observations are shaded in grey.

Furthermore, as already discussed above, this figure readily shows that the flux ratios change as a function of the spatial position in the disc of the galaxy and in the tail, which is suggestive of various excitation mechanisms at work in different regions. For instance, the front region has the highest [N II]-to-Hα ratio, while [O III] λ5007 is most strongly detected in the bright Hα knots along the tail. Furthermore, [O I] λ6300 emission is visibly stronger throughout the tail than in the main galaxy body.

This visual assessment of the data is more quantitatively supported by the integrated fluxes, listed in Table 2. The uncertainties on the line fluxes are computed from 100 bootstrap realizations of the median spectra. More specifically, the fitting procedure is repeated for each bootstrap realization, and we assume the 1σ confidence level of the measured line fluxes as the formal uncertainty. This approach, however, does not take into account the correlated noise contribution, which is estimated to be a factor of ∼2 for IFU observations where a similar number of pixels is combined (e.g. Förster Schreiber et al. 2009). For undetected lines, we quote the 3σ confidence level obtained from the standard deviation of the continuum values on both sides of each line.

In the next section, we will attempt to characterize the density, temperature, and metallicity of the gas, by means of emission line diagnostics leveraging a combination of spatially resolved maps and composite spectra.

4.3 Properties of the diffuse gaseous tails

4.3.1 Density

The electron density in the ionized gas can be measured, for instance, through collisional de-excitation in doublets of the same ion from different levels with comparable excitation energy. One such doublet is [S II] λ6716/λ6731. Unfortunately, the intensity ratio is only weakly sensitive to the density for $n_e < 10^2$ cm^{-3}, where collisional excitation is generally followed by photon emission. Moreover, in the case of ESO137−001, one of the [S II] lines falls on to a bright sky line, severely compromising the derived fluxes especially in the low-surface-brightness regions of the tail. For these reasons, we are forced to resort to other estimators for the gas density.

A crude order-of-magnitude estimate for the electron density can be obtained from the observed Hα luminosity, together with an estimate of the volume. More specifically, in equilibrium, the Hα luminosity in a given spatial region can be written as

$$L_{H\alpha} = n_e n_p \alpha^{eff}_{H\alpha} V f h \nu_{H\alpha}, \quad (1)$$

where n_e is the number density of electrons, n_p is the number density of protons (hydrogen ions), $\alpha^{eff}_{H\alpha}$ is the Hα effective recombination coefficient, V is the volume of the emitting region, f is the filling

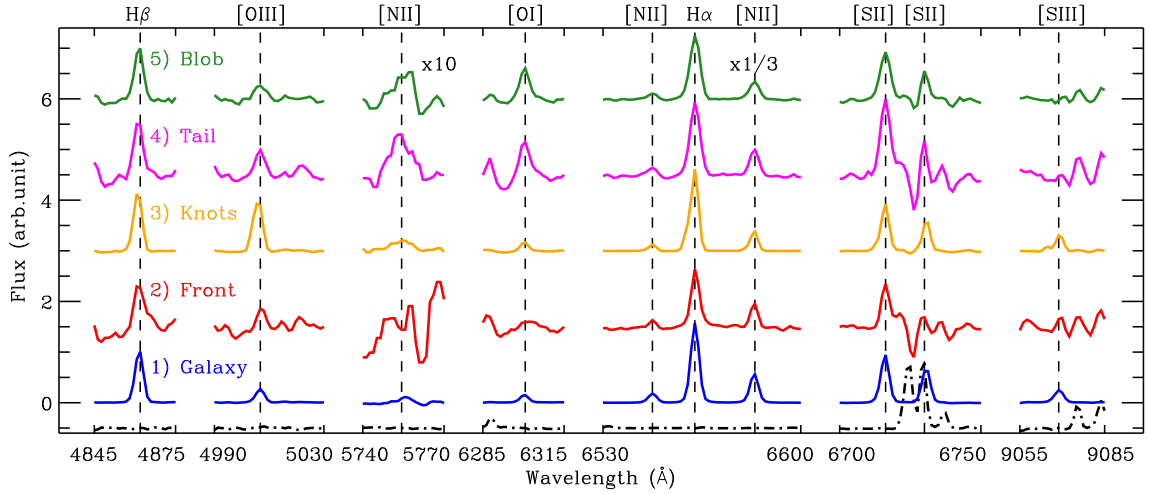

Figure 5. Co-added rest-frame spectra of the five regions of ESO137−001 shown in Fig. 4. The spectra are normalized to the Hβ intensity and shifted along the vertical axis to facilitate the comparison. Only the emission lines relevant to this study are shown. In case of [O III] and [O I] doublets, only the strongest line is shown. For visualization purposes, the Hα and [N II] complex have been scaled by a factor of 3, while the [N II] λ5755 is enhanced a factor of 10. The lowermost spectrum (dash–dotted line) is a night sky spectrum (not in scale) extracted from the data cube.

Table 2. Fluxes measured in the composite spectra of the five regions shown in Fig. 5. The values are normalized to the Hβ flux and are not corrected for dust extinction. We also report the dust extinction in units of A_V, measured from the Balmer decrement for the regions dominated by photoionization.

Line	λ_r (Å)	Δ_v^a (km s^{-1})	Region 1 (Disc)	Region 2 (Front)	Region 3 (Knots)	Region 4 (Tail)	Region 5 (Blob)
Hβ	4861.33	0	1.000 ± 0.022	1.000 ± 0.065	1.000 ± 0.013	1.000 ± 0.064	1.000 ± 0.020
[O III]	4958.91	<9 (3)	0.095 ± 0.006	<0.189	0.322 ± 0.066	0.111 ± 0.058	<0.141
[O III]	5006.84	<10 (4)	0.261 ± 0.007	0.252 ± 0.102	0.952 ± 0.174	0.392 ± 0.060	0.314 ± 0.023
[N II]	5754.64	<58 (3)	0.016 ± 0.009	<0.135	0.034 ± 0.008	0.065 ± 0.045	0.047 ± 0.019
[O I]	6300.30	<24 (3)	0.151 ± 0.005	<0.173	0.145 ± 0.010	0.694 ± 0.060	0.636 ± 0.018
[O I]	6363.78	<19 (1)	0.050 ± 0.005	<0.147	<0.051	<0.138	0.269 ± 0.026
[N II]	6548.05	<22 (3)	0.501 ± 0.017	0.322 ± 0.025	0.287 ± 0.056	0.467 ± 0.024	0.357 ± 0.010
Hα	6562.82	<20 (1)	4.529 ± 0.092	2.998 ± 0.038	3.954 ± 0.140	4.267 ± 0.040	3.984 ± 0.019
[N II]	6583.45	<24 (3)	1.604 ± 0.065	1.190 ± 0.036	0.928 ± 0.106	1.499 ± 0.032	1.107 ± 0.013
[S II]	6716.44	<23 (5)	0.921 ± 0.022	<0.174	0.745 ± 0.039	1.629 ± 0.116	1.056 ± 0.015
[S II]	6730.81	<20 (5)	0.651 ± 0.016	<0.219	0.470 ± 0.037	<0.297	0.422 ± 0.030
[S III]	9068.60	<16 (2)	0.249 ± 0.010	0.210 ± 0.055	0.241 ± 0.030	<0.216	<0.108
A_V			1.44 ± 0.09	–	1.02 ± 0.25	–	–

Note. [a]Absolute value of the largest offset peak centre relative to Hβ. The value in parentheses indicates the region where this occurs.

factor, h is the Planck constant, and $\nu_{H\alpha}$ is the frequency of the Hα transition.

For the geometry of the tail, we assume a cylinder with line-of-sight depth equal to the diameter in the plane of the sky. The diameter, as measured on the Hα image, is $D \sim 0.3$ arcmin throughout the entire length of the tail or about $D \sim 5.5$ kpc at the distance of ESO137−001. This value is ∼50 per cent larger than the diameter used by Sun et al. (2007), as the superior depth of the MUSE observations allows us to also detect the lower surface brightness components of the tail. In our calculation, we consider single spaxel with area A as individual regions. The filling factor is instead unconstrained. However, there is indication that the warm ionized gas in the tail can be very clumpy, as shown for instance in hydrodynamic simulations of ram-pressure stripping (e.g. Tonnesen, Bryan & Chen 2011). Thus, we assume $f = 0.05$, as in Sun et al. (2007). Finally, we assume that the gas is fully ionized ($n_e = n_p$) and $\alpha^{eff}_{H\alpha} = 1.17 \times 10^{-13}$ cm^3 s^{-1} (Osterbrock & Ferland 2006). As previously noted, the excitation mechanisms of the tail are unknown and the value of the recombination coefficient is uncertain. Moreover, the assumption of a cylindrical volume implies that the line-of-sight depth of the cylinder depends on the spatial position. However, our calculation aims to provide only an order-of-magnitude estimate for the gas density and other quantities, such as the filling factor, are likely to dominate the error budget in this calculation. Under these assumptions, manipulating equation (1) we obtain

$$n_e = \sqrt{\frac{L_{H\alpha}}{\alpha^{eff}_{H\alpha} A D f h \nu_{H\alpha}}}. \quad (2)$$

Fig. 6 shows the resulting map for the gas density obtained following equation (2), where H II regions have been excluded from the calculation. From the map, we find that the average density in the tail, although uncertain, is of the order of 0.3 cm^{-3}, in agreement with the estimate of Sun et al. (2007). Very similar densities are found by Yagi et al. (2007) and Fossati et al. (2012) in ram-pressure-stripped tails in the Coma cluster, once a common filling factor is assumed. As a cross-check, we also examine the composite spectrum of the tail, where the improved S/N also allows us to estimate the density with the direct method. In this case, we find an upper limit at $n_e \leq 1$ cm^{-3} typical for the low-density regime, which is again consistent with our spatially resolved measurement.

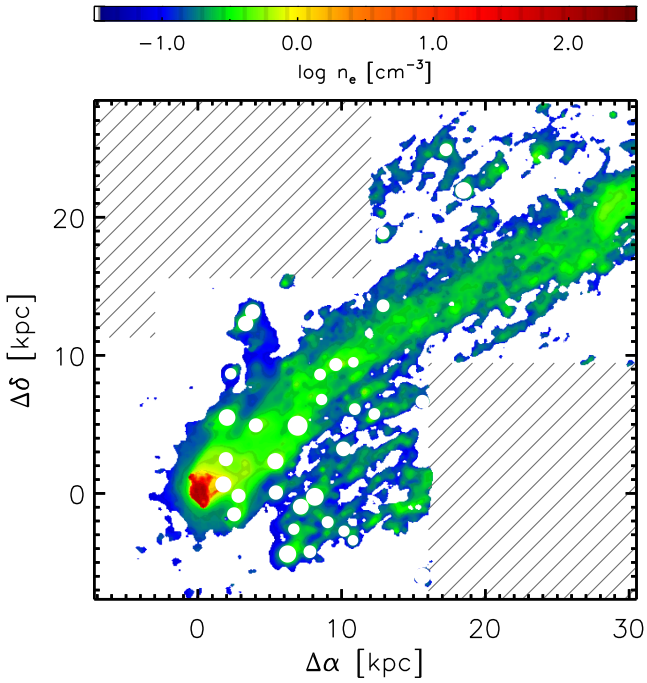

Figure 6. Map of the mean election density obtained from the Hα surface brightness and a cylindrical volume from the tail. A filling factor $f = 0.05$ is assumed. Areas not covered by MUSE observations are shaded in grey. The H II regions along the tail are excluded from the map.

In the nucleus, the S/N of both [S II] lines is high (see Fig. 5) and the density is in the intermediate regime where the doublet line ratio becomes a useful diagnostic of the n_e. We can therefore use the direct method, obtaining $n_e \sim 10^2$ cm^{-3}.

With an estimate for the density, we then compute the recombination time-scale for the ionized gas:

$$\tau_r = \frac{1}{n_e \alpha_A} \sim \frac{10^5}{n_e} \text{ yr}, \quad (3)$$

where α_A is the total recombination coefficient. At the high densities of the nucleus, the gas would recombine in less than 10^3 yr, and the observed emission arises from on-going star formation that

keeps the gas ionized. On the other hand, the gas in the tail can remain ionized up to ∼1 Myr following ionization. It is therefore interesting to consider whether the gas is being stripped as ionized and recombines in the tail, or whether other ionization mechanisms are needed to power the observed emission. The orbital study of Jachym et al. (2014) suggests an infall velocity of 3000 km s^{-1}, which means that material at ∼30 kpc has been stripped at least 10 Myr ago, assuming instantaneous acceleration of the gas. Thus, according to our crude estimate, only the inner part of the tail could be recombining after being stripped in an ionized phase. Other excitation mechanisms are at work in the full extent of the tail, as shown by simulations (Tonnesen & Bryan 2010). Clearly, the uncertainties on the density and thus in the recombination timescale hamper firm conclusions. Arguably, both recombination of stripped gas in the ionized phase and from gas excited *in situ* within the tail are powering the observed emission.

4.3.2 Electron temperature

The high S/N of the composite spectra allows the detection of emission lines that are suitable to measure the electron temperature of the gas in the galaxy and its tail. In principle, a few transitions like [O III], [N II], and [S III] could be used for this purpose, as emission lines from levels with different excitation energies fall into the optical window. However, given the wavelength coverage of our MUSE data, we are restricted to the use of [N II] for this calculation.

We use equation 5.5 in Osterbrock & Ferland (2006), and we assume that the density dependence in the denominator is negligible. The error introduced in making this assumption is 0.4 per cent in the nucleus where $n_e \sim 10^2$ cm^{-3}, and smaller elsewhere. The gas temperature is given by

$$T_e = \frac{2.5 \times 10^4 \text{ K}}{\ln(0.121 \times R_{[\text{N II}]})}, \quad (4)$$

where $R_{[\text{N II}]} = [\text{N II}]\lambda\lambda 6584, 6548/[\text{N II}]\lambda 5755$. In this calculation, we use observed line ratios not corrected for dust extinction, primarily because of our inability to derive the extinction curve especially in the tail and blob, where the ionization mechanisms are more uncertain. The values of T_e must therefore be taken as lower limits, given that $R_{[\text{N II}]}$ may in fact be lower than the value we measure. However, we checked that in the disc of the galaxy, where there is substantial extinction ($A_V \sim 1.44$ mag), the temperature would increase by only ∼6 per cent.

Clearly, the accuracy of this direct method is limited by the detection of the faint [N II] λ5755 line. In our composite spectra, we obtain marginal detections in all the regions, except the front. Fortunately, the wavelength where this line falls is clean from sky lines and we can attempt a measurement of the temperature even in a moderate-S/N regime. Robust fits are obtained by fixing the line width and centroid for all the [N II] lines, therefore avoiding spurious solutions for the faint [N II] λ5755 line. Bootstrap errors are used to derive the uncertainties for the electron temperatures. T_e are then $(0.96 \pm 0.19) \times 10^4$ K in the galactic disc, $(1.8 \pm 0.3) \times 10^4$ K in the stacked H II regions, and $(2.1 \pm 0.9) \times 10^4$ K, $(2.0 \pm 0.5) \times 10^4$ K for the tail and the blob, respectively. At face value, this measurement suggests that the gas in ESO137−001 has temperatures commonly seen in photoionized regions, perhaps with a hint of a lower value in the galactic disc compared to the tail or the H II regions. However, given the large uncertainties on the line flux and to lesser extent on the wavelength-dependent dust extinction, these values must be taken with caution. Deeper observations are thus required to confirm this result with higher S/N detection of the weak [N II] λ5755.

4.3.3 BPT diagnostics

In Section 4.1, we have shown two-dimensional maps of various line ratios. We now use the higher S/N composite spectra to study emission line ratios from the detections of Hβ, [O III], [O I], [N II], and Hα in the five characteristic regions of ESO137−001, defined in Fig. 4. Fig. 7 shows the BPT diagrams for these composite spectra, using the same colour coding as in Fig. 5. The 30 individual H II regions with detections in all the line ratios are also shown as small grey points. The error bars for the H II regions reflect the sample variance, while errors on the mean line ratios are of the size of the data point. The grey contours are obtained from the nuclear spectra of a random sample of Sloan Digital Sky Survey (SDSS) galaxies selected from the DR12 (Alam et al. 2015) data base at $0.03 < z < 0.1$, while the solid black line is the extreme starburst separation between photoionization and AGN/shock heating from Kewley et al. (2001). The dashed black line is the empirical division from Kauffmann et al. (2003) based on SDSS data. The thick solid lines highlight different fractions (from 0 to 1) of Hα flux contributed by shocks from models by Rich et al. (2011). Moreover, in Fig. 7 we show the line ratios obtained from the literature for extended ionized gas filaments (black stars) and compact star-forming knots (pink stars). Yagi et al. (2007) observed the tail behind D100, a galaxy in the Coma cluster. We average the line ratios of their slits along the tail, weighting by the Hα flux. Yoshida et al. (2012) observed several knots and extended diffuse emission filaments behind two galaxies infalling into the Coma cluster (IC4040 and RB199). Lastly, Merluzzi et al. (2013) observed a ram-pressure-stripped galaxy in the Shapley Supercluster, and we show the line ratios of their extraplanar ionized gas regions.

From the left-hand panel, it is clear that all the H II regions in the tail as well as the central galaxy reside in the locus occupied by gas photoionized by stars. These H II regions span a broad range of values in [O III] λ5007/Hβ, which is indicative of different ionization parameters. This result is consistent with the line ratios of H II regions observed in the tails of other ram-pressure-stripped galaxies from the literature (pink stars in Fig. 7). Thus, despite the extreme ram-pressure stripping suffered by ESO137−001, the star formation properties of the galaxy disc and of the H II regions embedded in the tail appear typical. Indeed, the stacked spectrum of the galactic disc is well within the region where most of local galaxy nuclei are found. It should be noted, however, that this analysis is restricted to the most bound parts of the ESO137−001 disc, as the star formation activity is completely truncated in the outer parts of the disc, where ram pressure has already removed the galaxy ISM and no Hα emission is found (see Paper I).

The galaxy front stands out as the region with the strongest [N II] contribution, which is however weak compared to the emission expected for a LINER or gas that is purely shock heated. This evidence, combined with the weak [O I] complicates the interpretation of which excitation mechanism is responsible for the gas emission. Indeed, at most 15 per cent of the excitation can be contributed by shocks in the front, according to the models by Rich et al. (2011). Moreover, the gas is kinematically cold in this region (Paper I), perhaps surprising in the presence of strong shocks moving through the gas. We therefore conclude that this region is mainly photoionized, with an elevated [N II]/Hα ratio but a faint [O III] emission indicative of a weak ionization parameter. As discussed above, however, we cannot rule out the contribution of shocks, as

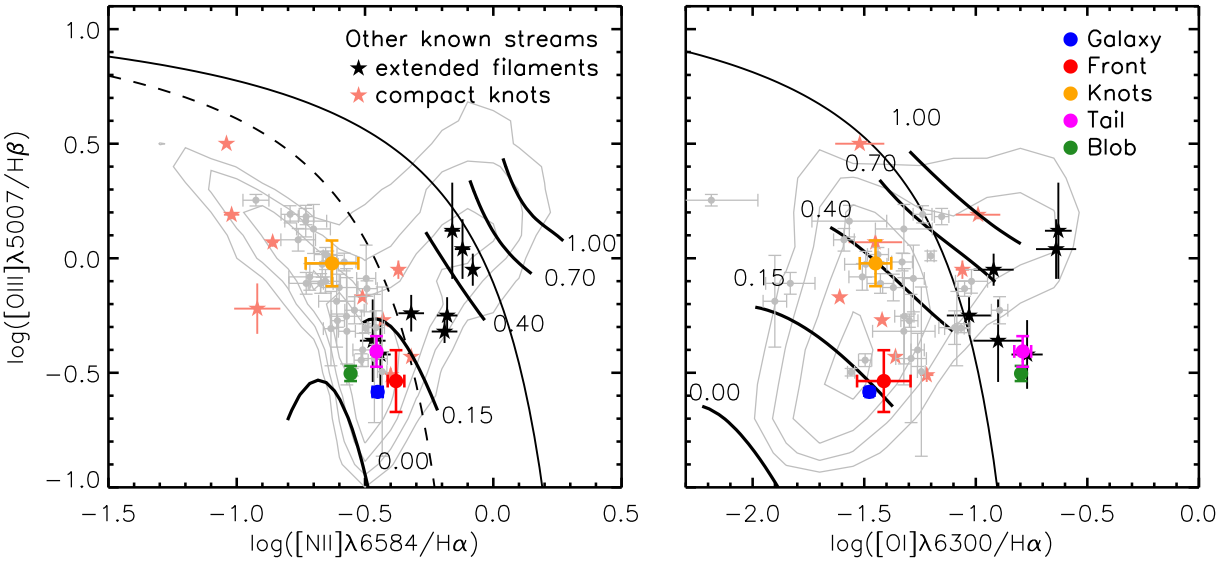

Figure 7. BPT diagrams for the composite spectra extracted from the five characteristic regions of ESO137−001. Data points are colour coded as in Fig. 5. Individual knots with robust detections in all the line ratios are also shown with small grey circles. The error bars shown for the composite knot spectrum reflect the sample variance, while the errors on the mean line ratios are of the size of the data point. Black (pink) stars are extended filaments (compact knots) from Yagi et al. (2007), Yoshida et al. (2012), and Merluzzi et al. (2013). The grey contours are obtained from the nuclear spectra of a random sample of SDSS galaxies at $0.03 < z < 0.1$. The solid black line is the extreme starburst separation between photoionization and AGN/shock heating from Kewley et al. (2001). The dashed black line is the empirical division from Kauffmann et al. (2003) based on SDSS data. Thick solid lines highlight different fractions (from 0 to 1) of Hα flux contributed by shocks from models by Rich et al. (2011).

the separation between a putative thin shock-dominated region and the bulk of the photoionized ISM in the ESO137−001 disc is poorly resolved in our observations. Moreover, composite spectra from extended regions are light weighted, and thus the measured fluxes near density discontinuities tend to be biased towards the brightest regions.

On the other hand, the tail and the bright blob in the outer tail show a contribution from very strong [O I] emitting gas, much beyond the locus typical for local galaxies. This evidence is consistent with the strength of [O I] in all the other ram-pressure-stripped tail observations collected from the literature. However, the [N II]/Hα ratio is weaker compared to most of the other tails, a fact that is difficult to reconcile with ordinary shock heating models. We note that the tail of ESO137−001 hosts several H II regions, especially in the secondary tail where lower values of [N II]/Hα can be found. In this case, we are tempted to conclude that such peculiar line ratios in the tail arise from a combination of recombination from photoionized gas (including gas that was stripped as ionized from the galaxy or that is ionized *in situ* by the H II regions) plus a shock contribution from the turbulence of the gas itself. This scenario is further supported by the high velocity dispersion of the gas along the tail (Paper I; Jachym et al. 2014).

4.4 Properties of the H II regions

In this section, we estimate the density, metallicity, and ionization parameters for regions where the gas is mainly photoionized by young stars, namely the H II regions embedded in the tail and the body of the ESO137−001 galaxy.

As a first step, we correct the emission line spectra for dust extinction using the Balmer decrement. Having restricted our analysis to purely photoionized regions, and with a temperature of $T \sim 10^4$ K, we can assume a theoretical Hα/Hβ ratio from case B recombination. This value depends only weakly on density and temperature and is 2.86 in the low density limit at $T = 10^4$ K (Osterbrock 1989). In case of density and temperature variations, the variation in the theoretical Hα/Hβ ratio is minimal. Therefore, the variations in the observed ratios can be mainly attributed to variations in the dust content. We compute the Balmer decrement as

$$C(\mathrm{H}\beta) = \frac{\log(2.86) - \log[\frac{F(\mathrm{H}\alpha)}{F(\mathrm{H}\beta)}]_{\mathrm{obs}}}{f(\mathrm{H}\alpha)}, \quad (5)$$

where $f(\mathrm{H}\alpha) = -0.297$ is the selective extinction of Hα relative to Hβ from the Galactic extinction law of Cardelli, Clayton & Mathis (1989), which we also use for the correction of all the observed emission lines. Under these assumptions, we express the attenuation in units of $A_V = 2.5 \times 0.86 \times C(\mathrm{H}\beta)$. A map of the extinction of the H II regions is given in the bottom panel of Fig. 8. The extinction is on average 1 mag, with substantial scatter from region to region, suggestive of varying dust content within the body and tail of this galaxy (and perhaps along the line of sight to it). No clear trends are visible with the position along the tail.

The density for the H II regions in the tail can be estimated following equation (1) but adopting a spherical geometry in which the volume is $V = 4\pi R^3/3$. In our observations, we cannot resolve the size of the individual H II regions and we assume a constant radius $R = 20$ pc (see Gutiérrez & Beckman 2010). Also for the H II regions, the filling factor is unknown and likely to be a function of radius (Cedrés et al. 2013). In this case, we assume $f = 1$ meaning that our estimates provide a lower limit for the local density of these H II regions. Although the uncertainty on the density is very large, we find $n_e \gtrsim 10^2$ cm^{-3}, at least two orders of magnitude denser than the diffuse gas in the tail.

With the dust-corrected spectra, we can infer the chemical abundance of the H II regions using photoionization modelling. The

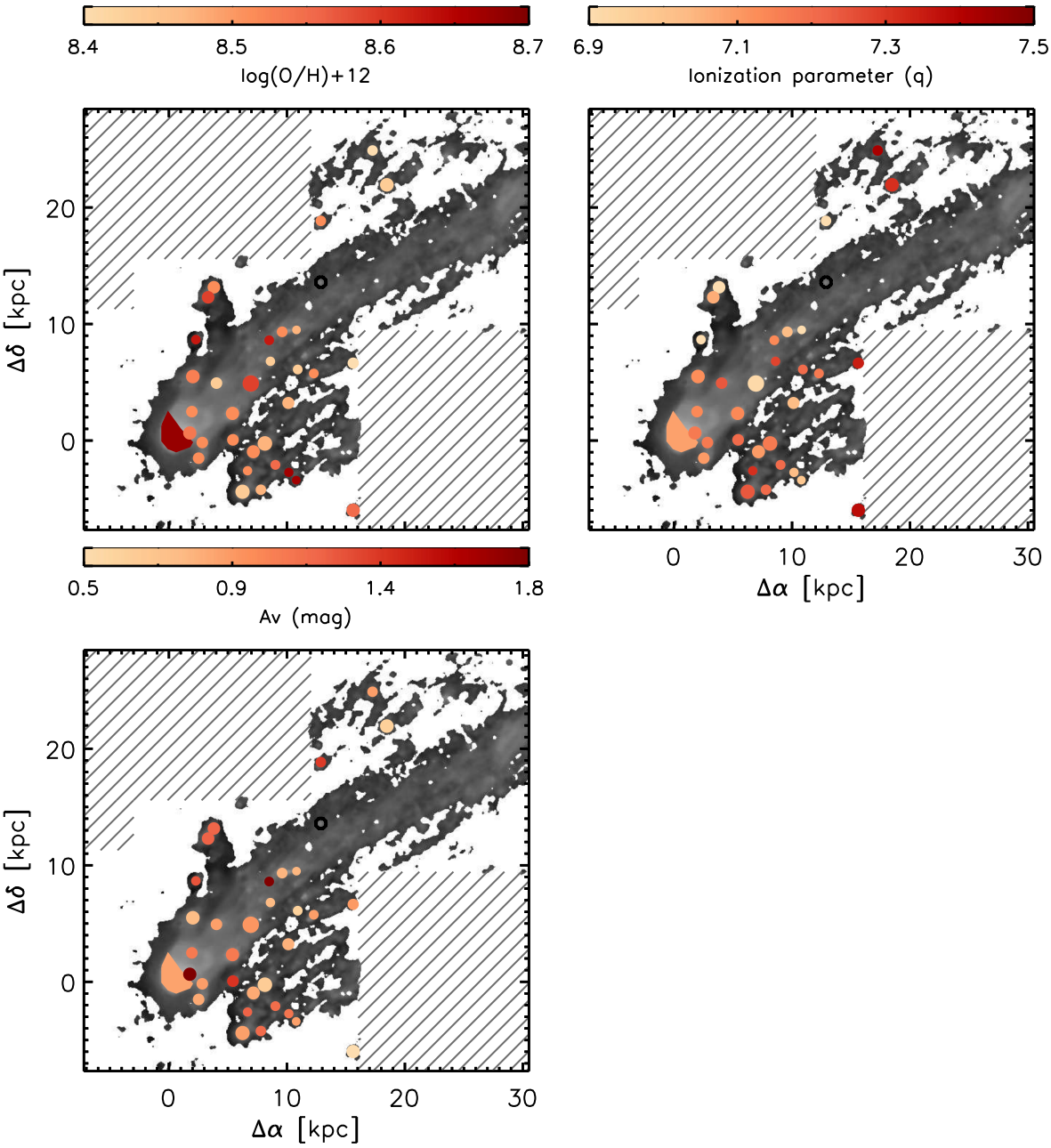

Figure 8. Top: maps of the gas phase metallicity and ionization parameter for the H II regions and the disc of ESO137−001 obtained from nebular emission lines fitting with the IZI code. Bottom: map of the dust extinction in the same regions, computed from the Balmer decrement. One H II region with insufficient S/N in Hβ is shown as an empty black circle. The Hα diffuse emission is shown in grey-scale as a reference for the position of the H II regions along the tail.

metallicity is of great importance to understand how the star formation proceeds in stripped tails, and how much of the stripped gas pollutes the intracluster environment. Another interesting parameter, a by-product of the metallicity analysis, is the ionization parameter (q), defined as the flux of ionizing photons per unit gas density.

In order to derive the gas phase metallicity (O/H) and ionization parameter of the gas, we use the IZI (Blanc et al. 2015) code to fit the observed nebular emission lines in our spectra against photoionization models. For this analysis, we use the input models from Kewley et al. (2001), who derive line fluxes from the MAPPINGS-III code with input stellar spectra computed using the STARBURST99 code (Leitherer et al. 1999). Those models are computed for a gas density $n_e = 350$ cm^{-3}, a constant star formation rate (SFR), and they assume a Salpeter (Salpeter 1955) initial mass function (IMF). The IZI code uses Bayesian statistics to derive the joint marginalized probability density function (PDF) for O/H and q. Here, we run the code with flat priors, with the exception of a handful of problematic cases. Indeed, during the analysis, we identify four H II regions for which the posterior PDF has multiple peaks for at least one of the parameters of interest. In these few cases, we impose a Gaussian prior on q which is motivated by the excellent linear correlation ($r = 0.91$) between q and the [O III] λ5007/Hβ ratio observed in the remaining H II regions where the PDFs are well behaved. We checked that the results do not change if we assume models with density $n_e = 10$ cm^{-3}, as data constrain only the ionization

parameter with a degeneracy between density and intensity of the ionizing radiation.

Maps of O/H and q are shown in the top panels of Fig. 8. We start by noting that the metallicity in the body of the galaxy is $\log(\mathrm{O/H}) + 12 \sim 8.65$, which is consistent with the determination $\log(\mathrm{O/H}) + 12 \sim 8.7$ by Sun et al. (2007), obtained using different data but the same suite of models. This agreement confirms the lack of systematic biases due to flux calibrations in the analysis. The uncertainty on the metallicity of individual H II regions is 0.1 dex as obtained from the widths of the posterior distributions. However, the use of a specific grid of models introduces an additional systematic uncertainty, which we estimate around 0.15 dex error by repeating the analysis with different models. Therefore, the metallicity is known with a quite large uncertainty.

The spatial variations we find in Fig. 8 are small and consistent with constant metallicity throughout the tail with an average value of $\log(\mathrm{O/H}) + 12 \sim 8.55 \pm 0.06$, which is 0.75 times the value assumed for the solar metallicity. A similar behaviour is seen for the ionization parameter, although uncertainties in individual measurements hamper firm conclusions on a spatial variation, if any is present.

Lastly, we convert the Hα de-reddened flux into an SFR using the Kennicutt (1998) calibration. The total SFR of the selected H II regions is $\mathrm{SFR} = 0.62 \pm 0.03\,\mathrm{M}_\odot\ \mathrm{yr}^{-1}$, in excellent agreement with the value $\mathrm{SFR} = 0.59\,\mathrm{M}_\odot\ \mathrm{yr}^{-1}$ found by Sun et al. (2007) using the same SFR calibration and a Salpeter IMF. This confirms once again the quality of the absolute flux calibration of the MUSE observations. We caution however that, because of the low intrinsic SFR of individual H II regions, a full treatment of the stochastic IMF sampling is likely required for a more precise measurement of the SFR (da Silva, Fumagalli & Krumholz 2014).

While there is no systematic trend of the physical properties of these H II regions with respect to their spatial location, the distribution of H II regions is in itself peculiar and traces the imprint of the formation mechanism. One third of the H II regions are found in leading edge of the secondary tail and they are among the brightest that we have observed in ESO137−001. Other H II regions are distributed along the main tail and only a few of them are found at a distance greater than 15 kpc from the galactic disc. Moreover, most of the H II regions are located in the inner part of the tail, where the velocity dispersion of the gas on scales larger than individual H II regions is low ($\sigma \sim$ 25–50 km s^{-1}). In fact, the most distant H II regions are not found in the primary tail, where we observe an increased velocity dispersion (Paper I). Rather, they reside in the diffuse gas in the northern part of our field of view, where the velocity dispersion is indeed low. If H II regions were formed in the galactic disc and stripped downstream by ram pressure, then they would be expected to lie anywhere in the tail. However, if instead the H II regions are formed *in situ* within the tail, then they are preferentially expected to reside where the gas is less turbulent, and the gas can cool and self-shield to form molecules.

This argument is complicated by age effects, as the stripped H II regions would progressively fade as the gas is accelerated to larger distances from the galaxy body. Further, some of the H II regions may not survive the violent stripping and hydrodynamic interactions with the hot ICM. However, another piece of evidence in favour of *in situ* formation, at least for some H II regions, comes from the analysis of Sun et al. (2007), who reported young ages <8 Myr for all the H II regions considered. If they were formed in the galaxy, then a clearer age gradient would be expected, as the galaxy moves in the cluster potential and the H II regions trail behind it. As we noted, also Sun et al. (2007) caution that older H II regions may have faded in the outer tail, below the depth of our observations.

5 SUMMARY AND CONCLUSIONS

In this paper, we have presented the analysis of the physical properties of the disc and stripped tail of ESO137−001, a galaxy that is infalling into the nearby Norma cluster at high velocity. Leveraging on the sensitivity and spatial resolution of MUSE observations, we have studied for the first time 2D maps of emission line ratios within a poster child of violent ram-pressure stripping.

Due to the complex interaction between different gas phases, several physical processes are likely involved in the ionization that powers the observed emission of the tail and the embedded H II regions. While we cannot fully disentangle each source of ionization, our analysis has provided new insight into the physical conditions of the emitting gas. Our results can be summarized as follows.

(1) Considering the tail, the analysis of line ratios shows high values of [N II]/Hα and [O I]/Hα. Thus, photoionization alone cannot be responsible for the observed emission, and the contribution of other mechanisms is required. A contribution from shocks is likely, also given the turbulent nature of the gas in the outer tail, but we cannot exclude thermal conduction with the hot ICM and MHD waves as other excitation mechanisms. At the same time, line ratios are not as strong as commonly seen in pure shock heating models, and the gas temperature of $(2.1 \pm 0.9) \times 10^4$ K is similar to that found in photoionized gas. Part of the emission, particularly at close separations from the galaxy, may originate from recombination of photoionized gas stripped from the main body of the galaxy. The electron density in the tail is indeed low, $n_\mathrm{e} \sim 0.3$ cm^{-3}, and thus the recombination time-scale is long enough to keep the gas ionized up to a few kpc downstream.

(2) The bulk of the front region where the galaxy ISM first collides with the hot ICM is not dominated by strong shocks, as [O I] is only weakly or mostly undetected in our observations. Line ratios are mostly consistent with photoionized gas, although with a higher [N II]/Hα ratio compared to the main body of the galaxy. We caution, however, that the front region is poorly resolved in our observations, and the separation with the bulk of the galaxy ISM is ambiguous.

(3) A large number of bright compact knots have been identified in the tail. These regions stand out because of their high [O III]/Hβ and low [N II]/Hα and [O I]/Hα ratios, fully consistent with the locus occupied by H II regions in the BPT diagram. These H II regions have densities $n_\mathrm{e} \gtrsim 10^2$ cm^{-3} and temperatures $(1.8 \pm 0.3) \times 10^4$ K. Thus, despite residing in ram-pressure-stripped tails, they exhibit usual properties, commonly observed in H II regions. By comparing the line ratios to a grid of photoionization models, we found a metallicity close to the solar value (∼0.7 solar), albeit with substantial scatter.

(4) By comparing the spatial position of the H II regions to the kinematic maps presented in Paper I, we found that the H II regions are preferentially located in regions where the gas is dynamically cool, with a velocity dispersion less than 25–50 km s^{-1}. Indeed, no H II regions are found in the outer part of the tail where Fumagalli et al. (2014) and Jachym et al. (2014) found a high degree of turbulence. Moreover, the young ages of these regions as well as the lack of any trend in the physical properties as the function of their position suggest that these H II regions have formed *in situ* from the stripped gas in the tail, as also concluded by previous studies of this and similar systems (Sun et al. 2007; Arrigoni Battaia et al. 2012;

Fossati et al. 2012). However, we cannot fully exclude selection biases that prevent us from detecting older H II regions stripped from the main body.

Our analysis represents the first attempt to characterize the rich physics of the ESO137−001 tail. In this work, we have primarily focused on the most common emission line diagnostics for shocks and photoionized gas. However, other processes such as thermal conduction and MHD waves may play a role in the excitation of the tail. Deeper observations of the full extent of the tail that have been recently obtained with MUSE, together with detailed radiative transfer models, will allow future explorations of other diagnostics (possibly including weak lines such as [Fe X]) that are necessary to gain a more complete understanding of the physics at work in ram-pressure-stripped tails.

Our study demonstrates the feasibility of detailed analyses of the properties of diffuse low-surface-brightness material with large-field-of-view IFUs on 8–10 m class telescopes. By targeting galaxies like ESO137−001, future observations will be able to provide key information on how gas is ablated from galaxies that are infalling into clusters of different richness and along different orbits. Moreover, by examining spatially resolved line ratios, these studies will inform on what mechanisms power the observed emission. In turn, this will shed new insight into the physics of star formation within the stripped material, a possible source of intracluster light and metals for the ICM. Future observations that target cluster galaxies or groups across a wide range of environments will thus yield a comprehensive view of how ram pressure shapes the formation of the red sequence in the local Universe.

ACKNOWLEDGEMENTS

It is a pleasure to thank Giulia Mantovani, Eva Wuyts, Trevor Mendel, Mark Krumholz, Audrey Galametz, and Gary Ferland for useful discussion. We thank the anonymous referee for his/her constructive comments. This work is based on observations made with ESO telescopes at the La Silla Paranal Observatory under programmes ID 60.A-9349(A) and ID 60.A-9303(A). M. Fossati and DJW acknowledge the support of the Deutsche Forschungsgemeinschaft via Project ID 3871/1-1. M. Fumagalli acknowledges support by the Science and Technology Facilities Council [grant number ST/L00075X/1]. For access to the data used in this paper, the KUBEVIZ line fitting software, and the IDL codes to process the MUSE data cubes, please contact the authors.

REFERENCES

Alam S. et al., 2015, ApJS, 219, 12
Allen M. G., Groves B. A., Dopita M. A., Sutherland R. S., Kewley L. J., 2008, ApJS, 178, 20
Arrigoni Battaia F. et al., 2012, A&A, 543, A112
Bacon R. et al., 2010, Proc. SPIE, 7735, 773508
Baldry I. K., Balogh M. L., Bower R. G., Glazebrook K., Nichol R. C., Bamford S. P., Budavari T., 2006, MNRAS, 373, 469
Baldwin J. A., Phillips M. M., Terlevich R., 1981, PASP, 93, 5
Balogh M. et al., 2004, MNRAS, 348, 1355
Bell E. F. et al., 2004, ApJ, 608, 752
Bertin E., Arnouts S., 1996, A&AS, 117, 393
Blanc G. A., Kewley L., Vogt F. P. A., Dopita M. A., 2015, ApJ, 798, 99
Blanton M. R., Moustakas J., 2009, ARA&A, 47, 159
Boissier S. et al., 2012, A&A, 545, A142
Boselli A., Gavazzi G., 2006, PASP, 118, 517
Boselli A., Gavazzi G., 2014, A&AR, 22, 74
Boselli A., Boissier S., Cortese L., Gil de Paz A., Seibert M., Madore B. F., Buat V., Martin D. C., 2006, ApJ, 651, 811
Boselli A., Boissier S., Cortese L., Gavazzi G., 2008, ApJ, 674, 742
Boselli A., Cortese L., Boquien M., Boissier S., Catinella B., Gavazzi G., Lagos C., Saintonge A., 2014, A&A, 564, A67
Byrd G., Valtonen M., 1990, ApJ, 350, 89
Cappellari M., Emsellem E., 2004, PASP, 116, 138
Cardelli J. A., Clayton G. C., Mathis J. S., 1989, ApJ, 345, 245
Catinella B. et al., 2013, MNRAS, 436, 34
Cedrés B., Beckman J. E., Bongiovanni Á., Cepa J., Asensio Ramos A., Giammanco C., Cabrera-Lavers A., Alfaro E. J., 2013, ApJ, 765, L24
Cortese L., Gavazzi G., Boselli A., Franzetti P., Kennicutt R. C., O'Neil K., Sakai S., 2006, A&A, 453, 847
Cortese L. et al., 2010a, A&A, 518, L49
Cortese L. et al., 2010b, A&A, 518, L63
Cortese L., Catinella B., Boissier S., Boselli A., Heinis S., 2011, MNRAS, 415, 1797
Cortese L. et al., 2012, A&A, 544, A101
Cowie L. L., Songaila A., Hu E. M., Cohen J. G., 1996, AJ, 112, 839
da Silva R. L., Fumagalli M., Krumholz M. R., 2014, MNRAS, 444, 3275
Dressler A., 1980, ApJ, 236, 351
Fabello S., Kauffmann G., Catinella B., Li C., Giovanelli R., Haynes M. P., 2012, MNRAS, 427, 2841
Ferland G. J., Fabian A. C., Hatch N. A., Johnstone R. M., Porter R. L., van Hoof P. A. M., Williams R. J. R., 2008, MNRAS, 386, L72
Ferland G. J., Fabian A. C., Hatch N. A., Johnstone R. M., Porter R. L., van Hoof P. A. M., Williams R. J. R., 2009, MNRAS, 392, 1475
Fitzpatrick E. L., 1999, PASP, 111, 63
Förster Schreiber N. M. et al., 2009, ApJ, 706, 1364
Fossati M., Gavazzi G., Boselli A., Fumagalli M., 2012, A&A, 544, A128
Fossati M. et al., 2013, A&A, 553, A91
Fumagalli M., Krumholz M. R., Prochaska J. X., Gavazzi G., Boselli A., 2009, ApJ, 697, 1811
Fumagalli M., Gavazzi G., Scaramella R., Franzetti P., 2011, A&A, 528, A46
Fumagalli M., Fossati M., Hau G. K. T., Gavazzi G., Bower R., Sun M., Boselli A., 2014, MNRAS, 445, 4335 (Paper I)
Gavazzi G., Pierini D., Boselli A., 1996, A&A, 312, 397
Gavazzi G., Boselli A., Mayer L., Iglesias-Paramo J., Vílchez J. M., Carrasco L., 2001, ApJ, 563, L23
Gavazzi G., Fumagalli M., Cucciati O., Boselli A., 2010, A&A, 517, A73
Gavazzi G., Fumagalli M., Fossati M., Galardo V., Grossetti F., Boselli A., Giovanelli R., Haynes M. P., 2013, A&A, 553, A89
Giovanelli R., Haynes M. P., 1985, ApJ, 292, 404
Gunn J. E., Gott J. R., III, 1972, ApJ, 176, 1
Gutiérrez L., Beckman J. E., 2010, ApJ, 710, L44
Henriksen M., Byrd G., 1996, ApJ, 459, 82
Hinshaw G. et al., 2013, ApJS, 208, 19
Jachym P., Combes F., Cortese L., Sun M., Kenney J. D. P., 2014, ApJ, 792, 11
Jaffé Y. L., Smith R., Candlish G. N., Poggianti B. M., Sheen Y.-K., Verheijen M. A. W., 2015, MNRAS, 448, 1715
Kapferer W., Sluka C., Schindler S., Ferrari C., Ziegler B., 2009, A&A, 499, 87
Kauffmann G. et al., 2003, MNRAS, 346, 1055
Kenney J. D. P., Tal T., Crowl H. H., Feldmeier J., Jacoby G. H., 2008, ApJ, 687, L69
Kennicutt R. C., Jr, 1983, AJ, 88, 483
Kennicutt R. C., Jr, 1998, ARA&A, 36, 189
Kewley L. J., Dopita M. A., Sutherland R. S., Heisler C. A., Trevena J., 2001, ApJ, 556, 121
Koopmann R. A., Haynes M. P., Catinella B., 2006, AJ, 131, 716
Lang P. et al., 2014, ApJ, 788, 11
Larson R. B., Tinsley B. M., Caldwell C. N., 1980, ApJ, 237, 692
Leitherer C. et al., 1999, ApJS, 123, 3

Mendel J. T., Simard L., Ellison S. L., Patton D. R., 2013, MNRAS, 429, 2212
Merluzzi P. et al., 2013, MNRAS, 429, 1747
Mok A. et al., 2013, MNRAS, 431, 1090
Moore B., Katz N., Lake G., Dressler A., Oemler A., 1996, Nature, 379, 613
Nishino S., Fukazawa Y., Hayashi K., 2012, PASJ, 64, 16
Noll S., Kausch W., Kimeswenger S., Barden M., Jones A. M., Modigliani A., Szyszka C., Taylor J., 2014, A&A, 567, A25
Osterbrock D. E., 1989, Astrophysics of Gaseous Nebulae and Active Galactic Nuclei. University Science Books, Mill Valley, CA
Osterbrock D. E., Ferland G. J., 2006, Astrophysics of Gaseous Nebulae and Active Galactic Nuclei, 2nd edn. University Science Books, Mill Valley, CA
Peng Y.-j. et al., 2010, ApJ, 721, 193
Postman M., Geller M. J., 1984, ApJ, 281, 95
Rich J. A., Kewley L. J., Dopita M. A., 2011, ApJ, 734, 87
Salpeter E. E., 1955, ApJ, 121, 161
Sarzi M. et al., 2006, MNRAS, 366, 1151
Schlafly E. F., Finkbeiner D. P., 2011, ApJ, 737, 103
Schlegel D. J., Finkbeiner D. P., Davis M., 1998, ApJ, 500, 525
Sivanandam S., Rieke M. J., Rieke G. H., 2010, ApJ, 717, 147
Smith R. J. et al., 2010, MNRAS, 408, 1417
Solanes J. M., Manrique A., García-Gómez C., González-Casado G., Giovanelli R., Haynes M. P., 2001, ApJ, 548, 97
Storey P. J., Zeippen C. J., 2000, MNRAS, 312, 813
Sun M., Jones C., Forman W., Nulsen P. E. J., Donahue M., Voit G. M., 2006, ApJ, 637, L81
Sun M., Donahue M., Voit G. M., 2007, ApJ, 671, 190
Sun M., Donahue M., Roediger E., Nulsen P. E. J., Voit G. M., Sarazin C., Forman W., Jones C., 2010, ApJ, 708, 946
Tonnesen S., Bryan G. L., 2010, ApJ, 709, 1203
Tonnesen S., Bryan G. L., 2012, MNRAS, 422, 1609
Tonnesen S., Bryan G. L., Chen R., 2011, ApJ, 731, 98
Vazdekis A., Sánchez-Blázquez P., Falcón-Barroso J., Cenarro A. J., Beasley M. A., Cardiel N., Gorgas J., Peletier R. F., 2010, MNRAS, 404, 1639
Weinmann S. M., van den Bosch F. C., Yang X., Mo H. J., 2006, MNRAS, 366, 2
Wilman D. J., Zibetti S., Budavári T., 2010, MNRAS, 406, 1701
Wilman D. J., Fontanot F., De Lucia G., Erwin P., Monaco P., 2013, MNRAS, 433, 2986
Woudt P. A., Kraan-Korteweg R. C., Lucey J., Fairall A. P., Moore S. A. W., 2008, MNRAS, 383, 445
Yagi M., Komiyama Y., Yoshida M., Furusawa H., Kashikawa N., Koyama Y., Okamura S., 2007, ApJ, 660, 1209
Yagi M. et al., 2010, AJ, 140, 1814
Yoshida M. et al., 2002, ApJ, 567, 118
Yoshida M., Yagi M., Komiyama Y., Furusawa H., Kashikawa N., Hattori T., Okamura S., 2012, ApJ, 749, 43

This paper has been typeset from a TEX/LATEX file prepared by the author.